J. Fluid Mech. (2007), *vol.* 585, *pp.* 305–322.
doi:10.1017/S0022112007006714 Printed in the United Kingdom

Supersonic scattering of a wing-induced incident shock by a slender body of revolution

A. V. FEDOROV[1], N. D. MALMUTH[2] AND V. G. SOUDAKOV[1]

[1]Department of Aeromechanics and Flight Engineering, Moscow Institute of Physics and Technology, Zhukovski, 140180, Russia

[2]Teledyne Scientific and Imaging Company, Thousand Oaks, CA 91360, USA

(Received 18 November 2005 and in revised form 30 March 2007)

The lift force acting on a slender body of revolution that separates from a thin wing in supersonic flow is analysed using Prandtl–Glauert linearized theory, scattering theory and asymptotic methods. It is shown that this lift is associated with multi-scattering of the wing-induced shock wave by the body surface. The local and global lift coefficients are obtained in simple analytical forms. It is shown that the total lift is mainly induced by the first scattering. Contributions from second, third and higher scatterings are zero in the leading-order approximation. This greatly simplifies calculations of the lift force. The theoretical solution for the flow field is compared with numerical solutions of three-dimensional Euler equations and experimental data at free-stream Mach number 2. There is agreement between the theory and the computations for a wide range of shock-wave strength, demonstrating high elasticity of the leading-order asymptotic approximation. Theoretical and experimental distributions of the cross-sectional normal force coefficient agree satisfactorily, showing robustness of the analytical solution. This solution can be applied to the moderate supersonic (Mach numbers from 1.2 to 3) multi-body interaction problem for crosschecking with other computational or engineering methods.

1. Introduction

Multi-body interaction applications include separation and carriage of various stage vehicles for supersonic flights as well as crew escape. Common approaches to predicting aerodynamic interactions are based on steady experiments using captive trajectory simulation (CTS) and large-scale computational fluid dynamics (CFD). In this connection, a variety of advanced numerical procedures have been developed for predicting unsteady aerodynamic loads (Belk, Janus & Whitfield 1987; Thoms & Jordan 1995; Prewitt, Belk & Maple 1999). Although these methods are useful in engineering applications, they should be complemented by approaches based on systematic approximation schemes that minimize empiricism, and are theoretically based as well as physics-based, and are developed from first principles (Malmuth 2005). This will help to assess the role of parameters and provide important insight into the flow physics. Namely, the models should describe various aerodynamic processes including: shock–body interaction; interactions with shear layers and mixed boundary; nonlinear effects of shock diffraction; non-uniformity of flow fields; and unsteady effects. This could be achieved by identifying key unit problems and solving them using a combined asymptotic and numerical approach (Malmuth 2005).

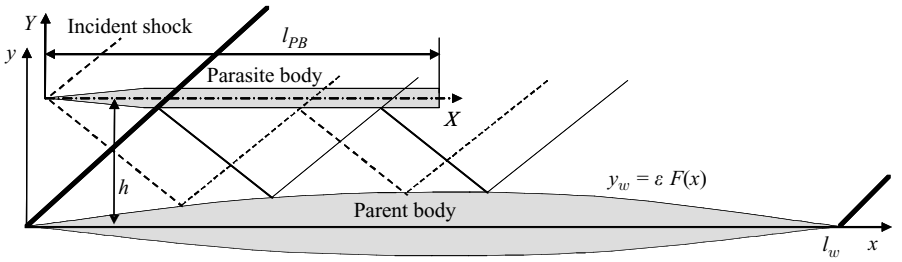

FIGURE 1. Schematic of wavetrains induced by a two-dimensional wing (solid lines) and by the PB nose (dashed lines).

Shalaev, Fedorov & Malmuth (2004) analysed effects of external flow non-uniformity and shock reflections on separation of a slender parasite body (PB) from a two-dimensional parent body (wing). This modelling, based on geometric acoustics, shows that reflections of the wing-induced shocks by the PB surface may significantly affect the lift force and pitching moment and lead to crucial changes of the PB trajectory. These findings motivated the analysis herein that evaluates the lift force associated with multi-scattering of a wing or planar body-induced shock by a slender body of revolution. In the present analysis, the nearly planar body shock is generated by a two-dimensional wing whose sharp leading edge is perpendicular to a moderately supersonic free stream.

The problem is treated using classical electromagnetic and acoustic scattering theory (Morse & Feshbach 1953; Bowman, Senior & Uslenghi 1969; Lependin 1978) as well as asymptotic methods (Van Dyke 1964; Cole & Cook 1986). Although acoustical and electromagnetic analyses such as those just cited are well known, their application to supersonic shock-wave scattering problems has not received significant attention.

In § 2, the problem is formulated within the framework of Prandtl–Glauert linearized supersonic theory. In § 3, analytical solutions are provided for the lift force induced by multiple scattering of a wedge bow shock incident on a cylindrical afterbody of a body of revolution whose axis of symmetry is aligned with the free-stream velocity vector. In § 4, theoretical predictions of the lift force coefficient and flow features are compared with numerical solutions obtained by integration of Euler equations. Comparison with the experimental data of Gapcynski & Carlson (1957) is discussed in § 5. The results are summarized in § 6.

2. Problem formulation

The physical problem is shown schematically in figure 1. A two-dimensional parent body (called a 'wing') is indicated in the figure having a length l_w^* and maximum thickness εl_w^* with $\varepsilon \ll 1$. Hereinafter, asterisks denote dimensional quantities. The parasite body of revolution (PB) is of length l_{PB}^* and consists of a slender sharp nose and a cylinder of radius a^*. It is assumed that the PB nose length is $l_N^* = O(l_{PB}^*)$, $l_{PB}^* = O(l_w^*)$, and the thickness ratio is $O(\varepsilon)$. In terms of the non-dimensional coordinates $(x, y, z) = (x^*, y^*, z^*)/l_{PB}^*$, the PB length is $l_{PB} = 1$ and $a = a^*/l_{PB}^* = O(\varepsilon)$. The PB axis is at a distance h^* from the wing centreline $y^* = 0$. The PB nose is located upstream from the interaction region; i.e. the nose-induced and wing-induced pressure waves are scattered by the cylindrical afterbody.

For this configuration, the free stream is disturbed by the wing and by the parasite body nose. The following cases are distinguished: Case 1. For $h = O(a) \ll 1$, multiple

reflections of the disturbances from the PB and wing surfaces lead to a wavetrain pattern. It is difficult to solve this problem analytically. Case 2. For $a \ll h \ll 1$, a wavetrain still occurs. However, the problem can be analysed using asymptotic methods with $\mu = a/2h$ treated as a small parameter. Case 3. For $a \ll h = O(1)$, one or few reflections of pressure waves may occur. Case 4. For $1 \ll h$, only one scattering occurs. Hereinafter, case 2 will be analysed in detail with the help of asymptotic methods. Applications of this solution to cases 3 and 4 are straightforward.

Formally, the Prandtl–Glauert (PG) limit $M_\infty = \text{fixed}$ $\varepsilon \to 0$ is considered, where M_∞ denotes the free-stream Mach number, which is greater than unity (typical cases are $1.2 \leqslant M_\infty \leqslant 3$, $\varepsilon \approx 0.1$). For this purpose, the non-dimensional flow potential asymptotic expansion in the aforementioned PG limit is introduced as (see, for example, Ashley & Landahl 1965; Loitsyansky 1970)

$$\Phi(x, y, z; M_\infty, \varepsilon) \equiv \frac{\Phi^*}{U_\infty^* l_{PB}^*} = x + \varepsilon\phi(x, y, z; \beta) + O(\varepsilon^2), \qquad \beta \equiv \sqrt{M_\infty^2 - 1} = O(1), \tag{2.1}$$

where ϕ is the perturbation potential.

For inviscid flow in the half space $y > 0$ (above the wing), ϕ is a solution of the PG approximation of the three-dimensional Euler equations (Ashley & Landahl 1965; Loitsyansky 1970), namely,

$$\beta^2 \partial_x^2 \phi - \left(\partial_y^2 \phi + \partial_z^2 \phi\right) = 0, \tag{2.2}$$

$$\partial_y \phi(x, 0, z) = F'(x), \quad y = 0, \tag{2.3}$$

$$\partial_n \phi = 0, \quad r = a, \tag{2.4}$$

where $F'(x) \equiv \mathrm{d}F/\mathrm{d}x$, ∂_n is a derivative normal to the body surface. The boundary conditions (2.3), (2.4) are formulated on the wing centreplane, $y = 0$, and the PB surface, $r = a$, respectively.

In the framework of linearized supersonic theory, the wing-induced and body-induced disturbances are treated independently. Because of three-dimensional relief, the conical waves emanating from the body nose are much weaker than the wing-induced plane waves. In the leading-order approximation, the perturbation potential relevant to the nose-induced disturbance is expressed as (see, for example, Ashley & Landahl 1965; Landau & Lifshitz 1986)

$$\varphi = 0, \qquad 0 < X < \beta r, \tag{2.5a}$$

$$\varphi = -\frac{1}{2\pi} \int_0^{X-\beta r} \frac{S'(\xi)\,\mathrm{d}\xi}{\sqrt{(X-\xi)^2 - \beta^2 r^2}}, \qquad X > \beta r, \tag{2.5b}$$

where $r = \sqrt{Y^2 + Z^2}$ is the radial coordinate measured from the body axis, $S(X) = \pi a_n^*(X)$ is the non-dimensional cross-sectional area of the body nose, and the coordinates X, Y are shown in figure 1. After reflection of these conical waves from the wing surface, only a small portion of the original disturbance propagates back to the parasite body. The first scattering of the PB-induced disturbance occurs at a distance from the PB nose at least twice as long as for the wing-induced disturbance (compare the wavetrain patterns shown in figure 1 by solid and dashed lines). Equations (2.5) indicate that the nose-induced potential is $\varphi = O(\mu^{1/2}\varepsilon^2)$ for a slender body of $a = O(\varepsilon)$. Since this potential is much smaller than the wing-induced potential $\varepsilon\phi$ in the expansion (2.1), the PB nose-induced disturbances are neglected in the following analysis.

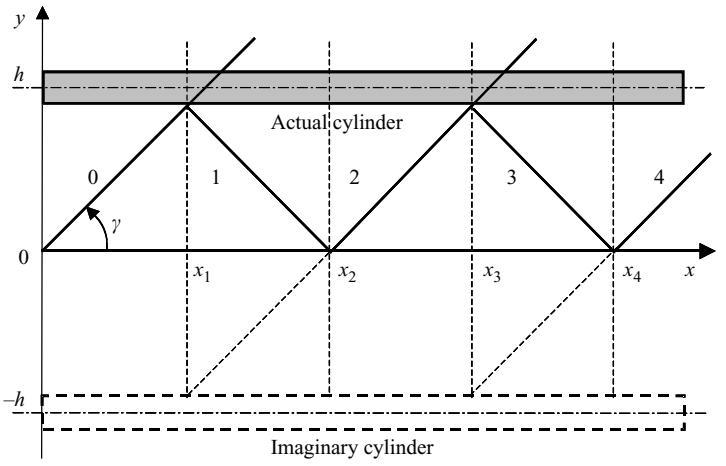

FIGURE 2. The wavetrain pattern between the wing plane $y=0$ and the cylinder.

3. Analysis

Herein the problem (2.2)–(2.4) is applied to the cylindrical afterbody where the body radius is $a=\text{const}$ (see figure 2). We exploit the hyperbolic nature of the linear equation (2.2) and restricted zones of dependence. The Mach wave lines (solid lines in figure 2) have the angles $\gamma=\pm\arcsin(1/M_\infty)$ and slopes $\mathrm{d}y/\mathrm{d}x=\pm\beta^{-1}$. The zero line starts from the wing leading-edge centreline $(x, y)=(0, 0)$ and represents the wing-induced shock wave, the first line represents the Mach wavelet due to the earliest reflection of the wing-induced disturbance by the cylinder, the second line is the Mach wavelet due to the earliest reflection from the wing centreplane, etc. In accord with this wavetrain pattern, the upper half-space $y\geqslant 0$ is divided into the sequence of strips: $x_{j-1}<x<x_j$, $j=1, 2, \ldots$, where $x_j=\beta(h-a)j$ (see figure 2). Hereinafter, we will formulate unit problems for these strips and solve them sequentially using the Laplace transform technique. The analysis will be focused on the lift force acting on the parasite body. In particular, our objective is to obtain the local, c_L, and the integral, C_L, lift coefficients defined as

$$c_L(x^*)\equiv\frac{2l^*_{PB}}{\rho^*_\infty U^{*2}_\infty\pi a^{*2}}\frac{\mathrm{d}L^*}{\mathrm{d}x^*},\qquad C_L(x^*)\equiv\frac{2L^*(x^*)}{\rho^*_\infty U^{*2}_\infty\pi a^{*2}}=\frac{1}{l^*_{PB}}\int_0^{x^*}c_L(x^*)\,\mathrm{d}x^*,\tag{3.1}$$

where L^* is the lift force directed along the y-axis.

3.1. *Solution in the region* 0

In the region $0<x<x_1$, the PB does not affect the flow in the leading-order approximation. The perturbation potential is induced by the wing only and governed by the problem (2.2)–(2.3). Taking the Laplace transform, $\bar\phi(p; y, z)=\int_0^\infty\phi(x, y, z)\mathrm{e}^{-px}\,\mathrm{d}x$, we obtain

$$\beta^2p^2\bar\phi-\left(\partial_y^2\bar\phi+\partial_z^2\bar\phi\right)=0,\tag{3.2}$$

$$\partial_y\phi(p;0,z)=p\bar F(p).\tag{3.3}$$

The solution of this problem is well known as

$$\bar\phi_0=-\frac{\bar F(p)}{\beta}\mathrm{e}^{-\beta py},\quad y>0.\tag{3.4}$$

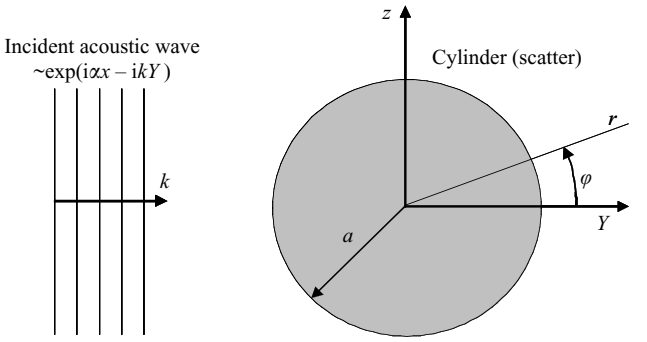

FIGURE 3. Incident plane wave scattered by a cylinder.

The inverse Laplace transform gives the simple-wave solution

$$\phi_0(x, y, z) = -\frac{1}{2\pi \mathrm{i}\beta} \int_{-\mathrm{i}\infty+c}^{+\mathrm{i}\infty+c} \bar{F}(p) \mathrm{e}^{p(x-\beta y)} \, \mathrm{d}p = -\frac{1}{\beta} F(x - \beta y). \tag{3.5}$$

With the substitutions $p = \mathrm{i}\alpha$ and $k = \beta\alpha$, this solution can be treated as a superposition of plane acoustic waves emanating from the plane $y = 0$ into the upper half-space

$$\phi_0(x, y, z) = -\frac{1}{2\pi} \int_{-\infty-\mathrm{i}c}^{+\infty-\mathrm{i}c} \beta^{-1} \bar{F}(\mathrm{i}\alpha) \mathrm{e}^{\mathrm{i}\alpha x - \mathrm{i}k y} \, \mathrm{d}\alpha. \tag{3.6}$$

Since the wing-induced disturbances do not reach the cylinder surface in the region 0, the lift in this region is zero, $c_L^{(0)}(x) = C_L^{(0)}(x) = 0$.

3.2. *Solution in the region* 1

In the region $x_1 < x < x_2$, the wing-induced waves (3.6) are scattered by the cylinder for the first time. Since the scattered waves do not reach the wing centreline in the region 1, the wing can be ignored and a unit problem can be considered that describes scattering of a plane wave of unit amplitude, $\mathrm{e}^{\mathrm{i}\alpha x - \mathrm{i}k y}$, by a cylinder into infinite space (figure 3). Multiplication of this unit problem solution by the amplitude $-(2\pi\beta)^{-1} \bar{F}(\mathrm{i}\alpha)$ (see (3.6)) and integrating over the entire spectrum of the wing-induced waves gives the perturbation potential and corresponding lift force associated with the first scattering.

In the polar coordinate system (r, φ), the potential of incident plane wave is

$$\phi_i = \exp(\mathrm{i}\alpha x - \mathrm{i}kY) = \exp(\mathrm{i}\alpha x - \mathrm{i}kr\cos\varphi), \tag{3.7}$$

where the coordinate Y is measured from the cylinder axis as shown in figure 3. The full perturbation potential including the incident wave and scattered waves is described by the classic solution (see, for example, Morse & Feshbach 1953; Lependin 1978)

$$\phi_s = \mathrm{e}^{i\alpha x} \sum_{m=0}^{\infty} j_m i^{-m} \left[J_m(kr) - \frac{J_m'(ka)}{H_m^{(2)\prime}(ka)} H_m^{(2)}(kr) \right] \cos m\varphi, \tag{3.8}$$

$$j_m = \begin{cases} 1, & m = 0, \\ 2, & m \geqslant 1, \end{cases}$$

where J_m are Bessel functions, $H_m^{(2)}$ are Hankel functions of the second kind, which satisfy the radiation condition for $kr \to \infty$. The corresponding pressure

perturbation is

$$P_s = -\partial_x \phi_s = \bar{P}_s(r, \alpha) \mathrm{e}^{\mathrm{i}\alpha x}, \tag{3.9}$$

$$\bar{P}_s(r, \alpha) = -\mathrm{i}\alpha \sum_{m=0}^{\infty} j_m i^{-m} \left[J_m(kr) - \frac{J'_m(ka)}{H_m^{(2)'}(ka)} H_m^{(2)}(kr) \right] \cos m\varphi. \tag{3.10}$$

On the cylinder surface, $r = a$, (3.10) is written as

$$\bar{P}_a \equiv \bar{P}_s(a, \alpha) = -\mathrm{i}\alpha \sum_{m=0}^{\infty} j_m i^{-m} \left[\frac{J_m(ka) H_m^{(2)'}(ka) - J'_m(ka) H_m^{(2)}(ka)}{H_m^{(2)'}(ka)} \right] \cos m\varphi. \tag{3.11}$$

The Wronskian $J_m(z) H_m^{(2)'}(z) - J'_m(z) H_m^{(2)}(z) = -2\mathrm{i}/(\pi z)$ (Abramowitz & Stegun 1964) leads to

$$\bar{P}_a = -\frac{2}{\pi k a} \alpha \sum_{m=0}^{\infty} j_m \mathrm{i}^{-m} \frac{\cos m\varphi}{H_m^{(2)'}(ka)}. \tag{3.12}$$

The component of lift-force coefficient induced by the elementary plane wave is expressed in the compact analytical form

$$\bar{c}_L^{(1)}(\alpha) = -\frac{2}{\pi a} \int_0^{2\pi} \bar{P}_a \cos\varphi \, \mathrm{d}\varphi = -\frac{8\mathrm{i}\alpha}{\pi k a^2 H_1^{(2)'}(ka)}. \tag{3.13}$$

Equation (3.6) indicates that the wing centreplane $Y = -h$ radiates plane waves of amplitude $-(2\pi\beta)^{-1} \varepsilon \bar{F}(\mathrm{i}\alpha) \mathrm{e}^{-ikh}$. Multiplying the solution (3.13) by this factor and integrating over the entire spectrum gives

$$c_L^{(1)}(x; h, a, \beta) = \frac{\varepsilon}{2\pi} \int_{-\infty - \mathrm{i}c}^{+\infty - \mathrm{i}c} \frac{\bar{F}(\mathrm{i}\alpha)}{\beta} \frac{8\mathrm{i}\alpha}{\pi k a^2 H_1^{(2)'}(ka)} \mathrm{e}^{\mathrm{i}\alpha x - \mathrm{i}kh} \, \mathrm{d}\alpha. \tag{3.14}$$

This solution can be written in terms of the inverse Laplace transform $L_p^{-1}[\bar{f}(p)]$. Introducing the Laplace variable $\bar{p} = \mathrm{i}\beta a \alpha$ and the local coordinate $\bar{x}_1 = (x - x_1)/(\beta a)$, yields

$$c_L^{(1)}(\bar{x}_1; \beta, a) = \frac{8\varepsilon}{\pi(a\beta)^3} L_{\bar{p}}^{-1} \left[\frac{\mathrm{i}\bar{F}(\bar{p}/\beta a) \mathrm{e}^{-\bar{p}}}{H_1^{(2)'}(-i\bar{p})} \right]. \tag{3.15}$$

Note that $c_L^{(1)}$ does not depend on the distance h, and it is valid for all cases given in § 2. If the parasite body has the variable radius $a(x)$, (3.15) serves as a local solution describing the lift due to shock-wave scattering in the local region $(x - x_1) = O(a)$. This solution can be matched with the outer solution representing the disturbance field far from the scattering region.

3.3. *Solutions in regions 2, 3, etc.*

In region 2, $x_2 < x < x_3$, disturbances induced by the first scattering spoil the boundary condition on the plane $y = 0$. This occurs first at the point $z = 0$, $x_2 = 2\beta(h - a)$ (see figure 2). Upstream from this point, the wing does not feel the presence of the parasite body. In order to compensate for perturbations induced by the PB on the wing centreplane downstream from x_2, the cylinder is imaged as shown in figure 2.

Imaginary disturbances emanating from the virtual cylinder represent waves reflected by the wing in the domain $x \geqslant x_2$. These waves are scattered by the PB again in the region $x \geqslant x_3$ (the second scattering). This process continues further and leads to third, fourth, etc. scatterings. In contrast to the first scattering, there are no exact analytical solutions describing higher scatterings. However, it is possible to

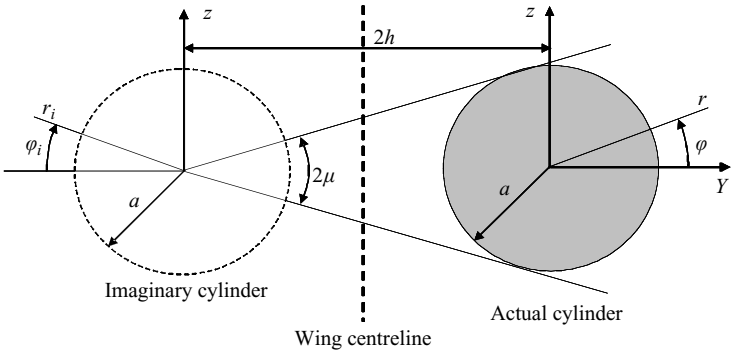

FIGURE 4. Cylindrical waves emanating from the imaging cylinder into the sector $\pi - \mu < \varphi_i < \pi + \mu$.

obtain asymptotic solutions for the case $h \gg a$ in which $\mu = a/(2h)$ is treated as a small parameter.

To treat the second scattering that occurs downstream from the point $x_3 = 3\beta(h-a)$, it is necessary to determine the disturbance field associated with the first scattering. Initially, consider the disturbance induced by the first scattering of an elementary plane wave $\sim e^{i\alpha x - iky}$. Its potential is given by the second term of (3.8)

$$\phi_s = -e^{i\alpha x} \sum_{m=0}^{\infty} j_m i^{-m} \frac{J'_m(ka)}{H_m^{(2)'}(ka)} H_m^{(2)}(kr_i) \cos m\varphi_i, \tag{3.16}$$

where (r_i, φ_i) are cylindrical coordinates related to the imaginary cylinder shown in figure 4. The potential (3.16) represents cylindrical waves emanating from the virtual cylinder. The actual cylinder sees only a small portion of these waves corresponding to the narrow segment $\pi - \mu < \varphi_i < \pi + \mu$ (see figure 4).

Herein, waves of $ka = O(1)$ in the coordinate system (x, Y, z) anchored in the actual cylinder are considered. For $kh \gg 1$ and $\pi - \mu < \varphi_i < \pi + \mu$, the Hankel function is approximated by the asymptotic expansion (Abramowitz & Stegun 1964)

$$H_m^{(2)} = \sqrt{\frac{1}{\pi kh}} \exp(-ikY - 2ikh) i^m \exp(i\pi/4)[1 + O(1/kh)]. \tag{3.17}$$

In the leading-order approximation, the disturbance (3.16) is a plane wave in the near-field region over the actual cylinder. The potential of this wave is

$$\phi_s = B(a, k, h) e^{i\alpha x - ikY - 2ikh}, \tag{3.18}$$

$$B(a, k, h) = -\sqrt{\frac{1}{\pi kh}} e^{i\pi/4} \sum_{m=0}^{\infty} i^{2m} j_m \frac{J'_m(ka)}{H_m^{(2)'}(ka)} \left[1 + O\left(\frac{1}{2kh}\right)\right]. \tag{3.19}$$

Scattering of the plane wave is described by the unit problem discussed in § 3.2. Using this similarity, the first-scattering solution (3.14) is adapted to treat the case of the second scattering as

$$c_L^{(2)}(x; h, a, \beta) = \frac{\varepsilon}{2\pi} \int_{-\infty - ic}^{+\infty - ic} B \frac{\bar{F}(i\alpha)}{\beta} \frac{8i\alpha}{\pi k a^2 H_1^{(2)'}(ka)} e^{i\alpha x - 3ikh} \, d\alpha. \tag{3.20}$$

Introducing the local variable $\bar{x}_2 = (x - x_3)/(\beta a)$ gives

$$c_L^{(2)}(\bar{x}_2; \beta, a) = \frac{8\varepsilon}{\pi(\beta a)^3} L_{\bar{p}}^{-1}\left[B(\bar{p})\frac{\mathrm{i}\bar{F}(\bar{p}/\beta a)\mathrm{e}^{-3\bar{p}}}{H_1^{(2)'}(-\mathrm{i}\bar{p})}\right], \tag{3.21a}$$

$$B(\bar{p}) = -\sqrt{\frac{2\mu}{\pi\bar{p}}}\sum_{m=0}^{\infty}\mathrm{i}^{2m+1} j_m \frac{J_m'(-i\bar{p})}{H_m^{(2)'}(-\mathrm{i}\bar{p})}[1 + O(\mu)]. \tag{3.21b}$$

The lift coefficient due to nth scattering is calculated in a similar way and expressed as

$$c_L^{(n)}(\bar{x}_n, \beta, a) = \frac{8\varepsilon}{\pi(a\beta)^3} L_{\bar{p}}^{-1}\left[B^{n-1}\frac{\mathrm{i}\bar{F}(\bar{p}/\beta\alpha)}{H_1^{(2)'}(-\mathrm{i}\bar{p})}\mathrm{e}^{-(2n-1)\bar{p}}\right], \tag{3.22a}$$

$$\bar{x}_n = (x - x_{2n-1})/(\beta a). \tag{3.22b}$$

Since the problem is linear, the streamwise distribution of the local lift coefficient is a sum of the functions $c_L^{(n)}(\bar{x}_n)$. This leads to the final form of asymptotic solution

$$c_L(x; \beta) = \frac{8\varepsilon}{\pi(\beta a)^3}\sum_{n=1}^{\infty}\mu^{(n-1)/2} D^{(n)}(\bar{x}_n), \tag{3.23a}$$

$$D^{(n)}(\bar{x}_n) = L_{\bar{p}}^{-1}\left[A^{n-1}\frac{\mathrm{i}\bar{F}(\bar{p}/\beta a)}{H_1^{(2)'}(-\mathrm{i}\bar{p})}\mathrm{e}^{-(2n-1)\bar{p}}\right], \tag{3.23b}$$

$$A = -\sqrt{\frac{2}{\pi\bar{p}}}\sum_{m=0}^{\infty}\mathrm{i}^{2m+1} j_m \frac{J_m'(-\mathrm{i}\bar{p})}{H_m^{(2)'}(-\mathrm{i}\bar{p})}[1 + O(\mu)]. \tag{3.23c}$$

Note that the second and higher terms of (3.23*a*), which represent the local lift induced by the second and higher scatterings, are given in the leading-order approximation with respect to μ.

4. Solution for a sharp wedge and comparison with numerical solutions

Since the non-dimensional body radius $a = O(\varepsilon)$ is small, the function $\bar{F}(\bar{p}/\beta a)$ can be approximated by its asymptotic expansion for large argument. For a wing with sharp leading edge, this expansion reads

$$\bar{F}(\bar{p}/\beta a) = a^2\beta^2/\bar{p}^2 + O((a\beta/\bar{p})^3). \tag{4.1}$$

The leading-order term corresponds to the shape function $F(x) = x$ representing a sharp wedge that approximates the wing nose. This motivates us to consider the sharp-wedge case in detail.

4.1. *Distribution of local lift force*

In the sharp-wedge case, the solution (3.23) is written as

$$c_L(x; \beta) = \frac{8\varepsilon}{\pi a\beta}\sum_{n=1}^{\infty}\mu^{(n-1)/2} G^{(n)}(\bar{x}_n), \tag{4.2a}$$

$$G^{(n)}(\bar{x}_n) = L_{\bar{p}}^{-1}\left[A^{n-1}\frac{\mathrm{e}^{-(2n-1)\bar{p}}}{\bar{p}^2 H_1^{(2)'}(-\mathrm{i}\bar{p})}\right], \tag{4.2b}$$

where the functions $G^{(n)}(\bar{x}_n)$ do not depend on parameters of the problem and can be calculated once and for all. These calculations were performed using standard

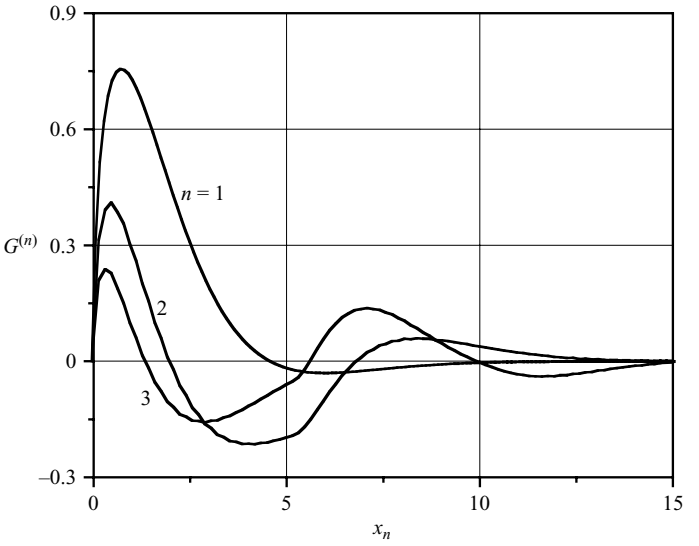

FIGURE 5. Functions $G^{(n)}(\bar{x}_n)$ relevant to the local lift coefficient due to the first ($n = 1$), second ($n = 2$) and third ($n = 3$) scatterings, here $\bar{x}_n$ is denoted as x_n.

routines of the Netlib library. Figure 5 shows the functions $G^{(n)}(\bar{x}_n)$, which can be treated as normalized local lift-force coefficients, for first, second and third scatterings. The maximum of $G^{(1)}(\bar{x}_1)$ is located at the point $\bar{x}_1 \approx 0.6$ that is rather close to the initial point $\bar{x}_1 = 0$, at which the leading-edge shock crosses the cylinder. The function $G^{(1)}(\bar{x}_1)$ rapidly attenuates as $\bar{x}_1$ increases. This trend indicates that the lift due to the first scattering is concentrated near the station $x = \beta h$. As the scattering number n increases, the maximum of $G^{(n)}(\bar{x}_n)$ decreases which leads to faster convergence of the asymptotic series (4.2*a*). Apparently the length of the scattering region increases with n, and the local lift distribution becomes more oscillatory.

4.2. *Total lift force*

According to (3.1), the integral lift coefficient is expressed as

$$C_L = 4\varepsilon \left[\sum_{n=1}^{\infty} \mu^{(n-1)/2} \frac{2}{\pi} \int_0^{\bar{x}_n} G^{(n)}(\bar{x}_n)\, \mathrm{d}\bar{x}_n \right]. \tag{4.3}$$

Consider the integral

$$I^{(1)}(\bar{x}_1) \equiv \frac{2}{\pi} \int_0^{\bar{x}_1} G^{(1)}(\bar{x}_1)\, \mathrm{d}\bar{x}_1$$

associated with the first-scattering contribution. Using the relation

$$L_p \left[\int_0^x f(x')\, \mathrm{d}x' \right] = p^{-1} \bar{f}(p)$$

and (4.2*b*) at $n = 1$, we obtain

$$I^{(1)}(\bar{x}_1 \to \infty) = \lim_{\bar{x}_1 \to \infty} \left[L_{\bar{p}}^{-1}(\bar{p}^{-1} \bar{G}^{(1)}(\bar{p})) \right]. \tag{4.4}$$

Asymptotic behaviour of $I^{(1)}$ for large $\bar{x}_1$ is determined by the inverse Laplace transform of $\bar{p}^{-1}\bar{G}^{(1)}(\bar{p})$ for small $|\bar{p}|$. The approximation of Hankel function

(Abramowitz & Stegun 1964)

$$H_1^{(2)'} = -\mathrm{i}\frac{2}{\pi z^2} + \cdots, \quad z \to 0, \tag{4.5}$$

gives

$$\bar{p}^{-1}\bar{G}^{(1)}(\bar{p}) = \frac{\mathrm{i}e^{-\bar{p}}}{\bar{p}^3 H_1^{(2)'}(-\mathrm{i}\bar{p})} = \tfrac{1}{2}\pi\bar{p}^{-1} + \cdots, \quad \bar{p} \to 0. \tag{4.6}$$

Taking the inverse Laplace transform of (4.6) and substituting the result into (4.4), we obtain $I^{(1)}(\infty) = 1$. Thus, the first scattering induces the total lift force, which is concentrated near the station $x = \beta h$ and expressed in simple form

$$C_L^{(1)}(\infty) = 4\varepsilon. \tag{4.7}$$

The lift force due to the second scattering is associated with the asymptotic behaviour of the integral

$$I^{(2)}(\bar{x}_2) \equiv \frac{2}{\pi}\int_0^{\bar{x}_2} G^{(2)}(\bar{x}_2)\,\mathrm{d}\bar{x}_2,$$

which has the Laplace transform

$$\bar{I}^{(2)}(\bar{p}) = \frac{2}{\pi}\frac{\mathrm{i}Ae^{-3\bar{p}}}{\bar{p}^3 H_1^{(2)'}(-\mathrm{i}\bar{p})}, \tag{4.8}$$

where A is given by (3.23c). Using expansions of Bessel and Hankel functions for small arguments (Abramowitz & Stegun 1964)

$$J_0'(z) = -\tfrac{1}{2}z + O(z^3),\ J_m'(z) = m\left(\tfrac{1}{2}z\right)^{m-1}\left(\frac{1}{\Gamma(m+1)} + O(z^2)\right),\ m = 1, 2, \mathrm{K}, \tag{4.9}$$

$$H_0^{(2)'}(z) = -\frac{2\mathrm{i}}{\pi z} + \cdots,\ H_m^{(2)'}(z) = -\frac{m}{\mathrm{i}\pi}\frac{2^m\Gamma(m)}{z^{m+1}} + \cdots, m = 1, 2, \mathrm{K}, \tag{4.10}$$

we obtain $A = const \times \bar{p}^{3/2}$ as $\bar{p} \to 0$. This gives $\bar{I}^{(2)}(\bar{p}) = const \times \bar{p}^{1/2}$ as $\bar{p} \to 0$, and

$$I^{(2)}(\bar{x}_2) = \frac{const}{\sqrt{\bar{x}_2}} \to 0, \bar{x}_2 \to \infty. \tag{4.11}$$

Thus, the total lift induced by the second scattering is $C_L^{(2)}(\infty) = 0$. Performing similar analysis for higher scatterings reveals that $I^{(n)}$ tends to zero with higher rates, and the corresponding lift coefficient is $C_L^{(n)}(\infty) = 0$.

We conclude that the total lift coefficient due to multiple scatterings of the wedge-induced shock by a long cylinder is localized at the station $x = \beta h + O(a)$ and is equal to $C_L(\infty) = 4\varepsilon$. This lift is predominantly generated by the first scattering. The second, third, etc. scatterings do not contribute to the lift force in the leading-order approximation with respect to ε.

Figure 6 shows the integrals $I^{(n)}(\bar{x}_n)$ for $n = 1, 2, 3$. The lift force is concentrated in the range $x - x_1 \sim 10\beta a$. Contributions from higher scatterings are shifted downstream since $x = \beta a\bar{x}_n + (2n-1)\beta(h-a)$, and are appreciable in the regions $\sim 15\beta a$. This indicates that a parasite body of finite length may experience the lift, which is substantially different from $C_L(\infty) = 4\varepsilon$. Moreover, the result may be affected by nonlinear interactions (when ε is not sufficiently small) and by multiple scatterings between closely spaced bodies (when μ is not sufficiently small). This motivated us to perform numerical experiments using a three-dimensional Euler solver and compare numerical solutions with the theoretical one.

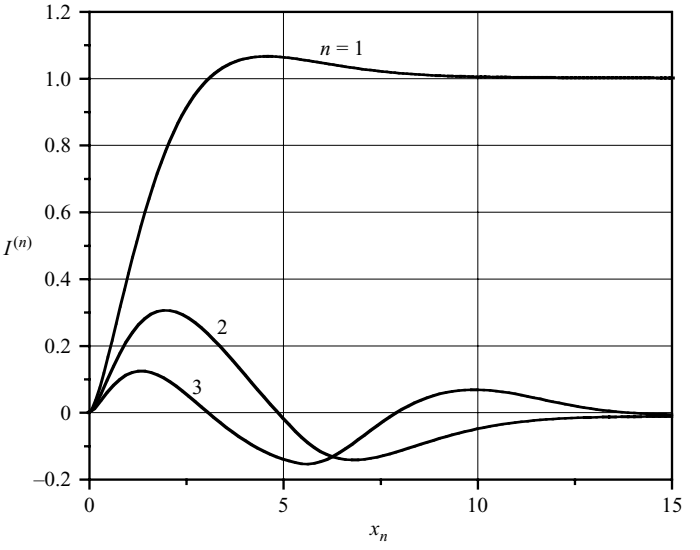

FIGURE 6. Integrals $I^{(n)}(\bar{x}_n)$ at $n = 1, 2, 3$, here $\bar{x}_n$ is denoted as x_n.

4.3. *Comparisons with numerical solutions*

Numerical solutions have been obtained using an implicit finite-volume method. The three-dimensional Euler equations were approximated by a conservative scheme. The flux vector was evaluated by an upwind flux-difference splitting (Roe 1986). The MUSCL algorithm is applied with the third-order TVD space discretization (Chakravarthy & Osher 1985). An Euler implicit discretization in time of the governing equations is combined with a Newton-type linearization of the fluxes to obtain the system of algebraic equations (Weiss, Maruszewski & Smith 1997). This system was solved using a point Gauss–Seidel scheme. The time marching proceeds until a steady-state solution sets in.

The bottom boundary of the computational domain coincides with the wedge surface of the angle α, $\varepsilon = \tan\alpha$. On this boundary and on the cylinder surface, the no-penetration condition is imposed. On the upper and inflow boundaries, dependent variables correspond to undisturbed free stream. On the outflow boundary, extrapolation of dependent variables provides 'soft' conditions. The flow symmetry conditions are imposed on the vertical plane passing through the cylinder axis. On the side boundary, which is parallel to the symmetry plane, non-reflecting boundary conditions are used. The computational domain has a length of $l_x = 35a$, the distance from the cylinder axis to the bottom boundary is $20a$, and from the symmetry plane $z = 0$ to the side boundary is $40a$. The computational grid has a cylindrical configuration with 150 cells in the x-direction, 110 cells in the radial direction and 120 cells in the azimuth direction (the total number of grid nodes is approximately 2×10^6).

The side view of pressure contours on the symmetry plane and on the cylinder surface are shown (figure 7*a*) for the case $M_\infty = 2$, $h = 7a$, $\alpha = 2°$. The wedge-induced shock wave is scattered by the cylinder, reflected by the wedge and scattered again; i.e. the computational domain covers the first and second scatterings. Figure 7(*b*) shows the front view to the cross-plane $x = 23a$ located slightly upstream from the second-scattering region. The cylinder generates waves producing a complex

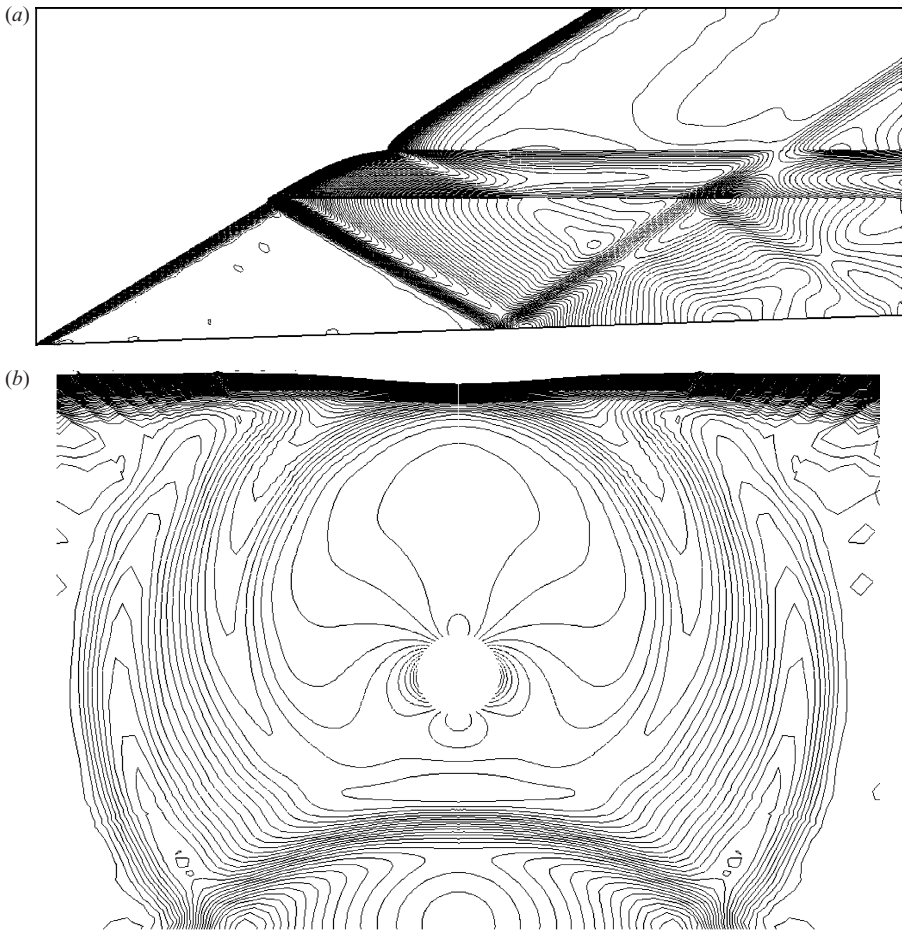

FIGURE 7. Fragment of pressure contours on the symmetry plane and on the cylinder surface (*a*) side view, $h = 7a$, $\alpha = 2^\circ$, $0 \leqslant x \leqslant 35a$, flow from left to right; (*b*) front view, $h = 7a$, $\alpha = 2^\circ$, $x = 23a$.

three-dimensional pressure field that gives a non-uniform pressure distribution on the cylinder surface. Despite this complexity, the normalized local lift due to the first scattering agrees well with the theoretical one (figure 8). Note that the initial point $x_1 = \beta(h - a)$ predicted by the linear theory, is shifted downstream with respect to the corresponding point of the numerical solution, because the nonlinear effect leads to a slight increase of the wedge-induced shock angle. This discrepancy is easily compensated for by using accurate analytical relations for the shock wave angle including nonlinear terms.

In figure 9, comparison of the lift force coefficients due to the first scattering indicates that the leading-order linear theory is quite robust. The discrepancy increases slowly with the wedge angle and does not exceed 8% at $\alpha = 8^\circ$.

Figure 10 illustrates the pressure field for a relatively small distance $h = 3a$ associated with multiple scatterings. The corresponding distribution of the normalized local lift coefficient $G(x) = \pi a \beta c_L(x)/8\varepsilon$ is shown in figure 11. The theoretical solution (solid line), which includes contributions from the first three scatterings, is expressed

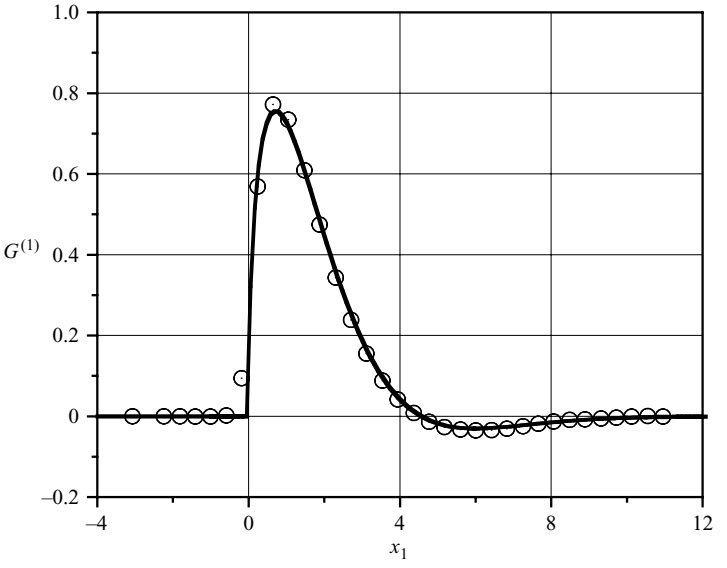

FIGURE 8. Normalized local lift coefficient $G^{(1)}(\bar{x}_1)$ due to the first scattering; solid line, theory; symbols, CFD solution for $M_\infty = 2$, $\alpha = 2°$, $h = 7a$, here $\bar{x}_1$ is denoted as x_1.

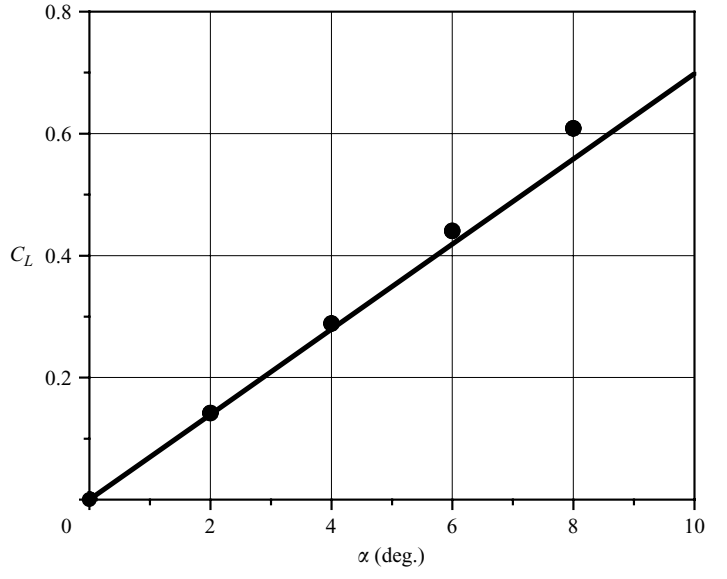

FIGURE 9. The total lift coefficient $C_L(\infty)$ due to first scattering as a function of the wedge angle $\alpha = \tan^{-1}\varepsilon$; solid line, theory; symbols, CFD solution for $M_\infty = 2$, $h = 7a$.

from (4.2*a*) as

$$G(x) = \sum_{n=1}^{3} \mu^{(n-1)/2} G^{(n)}(\bar{x}_n). \tag{4.12}$$

This solution is very close to the numerical one (symbols) despite of the not-so-small value of $\mu = 1/6$. Figure 12 shows the deviation of the total lift coefficient from the theoretical one versus the normalized distance h/a. The relative discrepancy is about

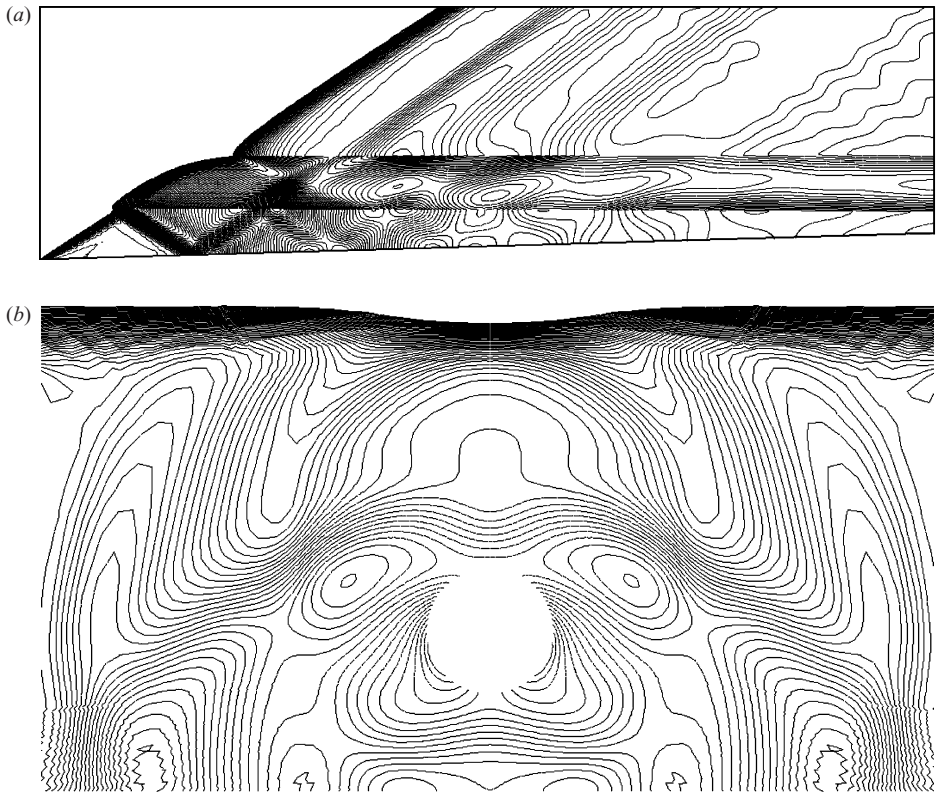

FIGURE 10. Fragment of pressure contours on the symmetry plane and on the cylinder surface (*a*) side view, $h = 3a$, $\alpha = 2^\circ$, $0 \leqslant x \leqslant 35a$, flow from left to right; (*b*) front view, $h = 3a$, $\alpha = 2^\circ$, $x = 13a$.

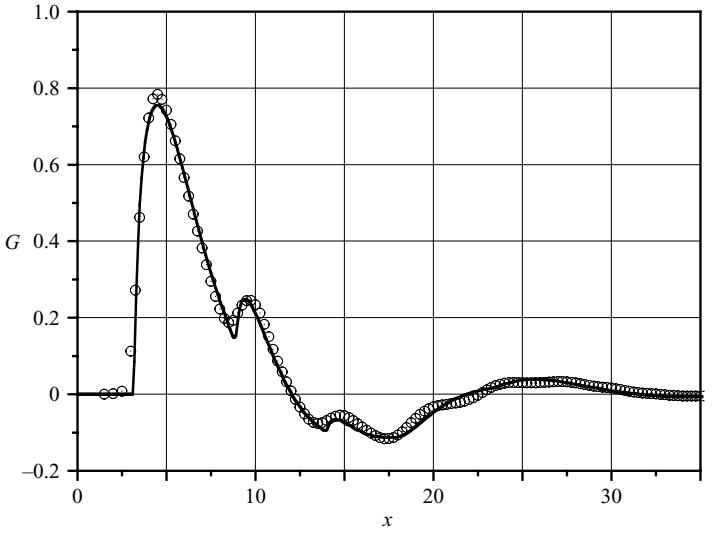

FIGURE 11. Normalized local lift coefficient $G(x)$; solid line, theory accounting for three scatterings; symbols, CFD solution for $M_\infty = 2$, $\alpha = 2^\circ$, $h = 3a$.

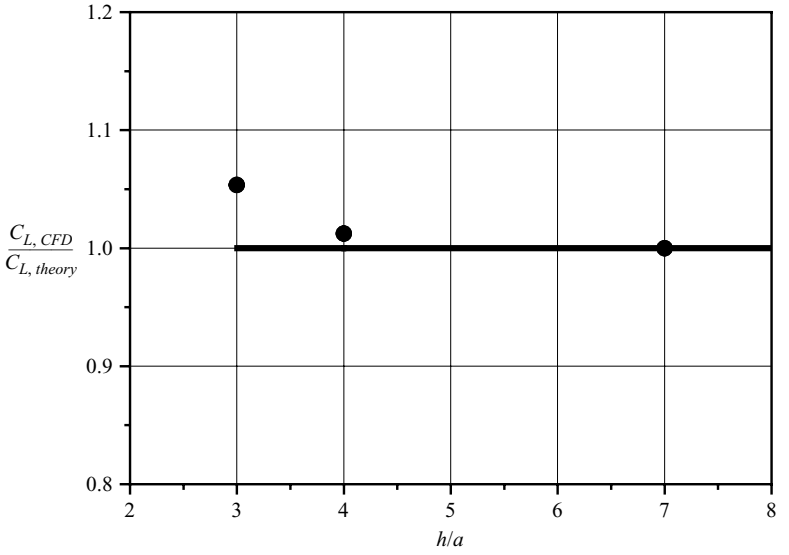

FIGURE 12. Relative deviation of the total lift coefficient predicted by CFD from the theoretical one versus the normalized distance h/a; $M_\infty = 2$, $\alpha = 2°$, $l_x = 35a$.

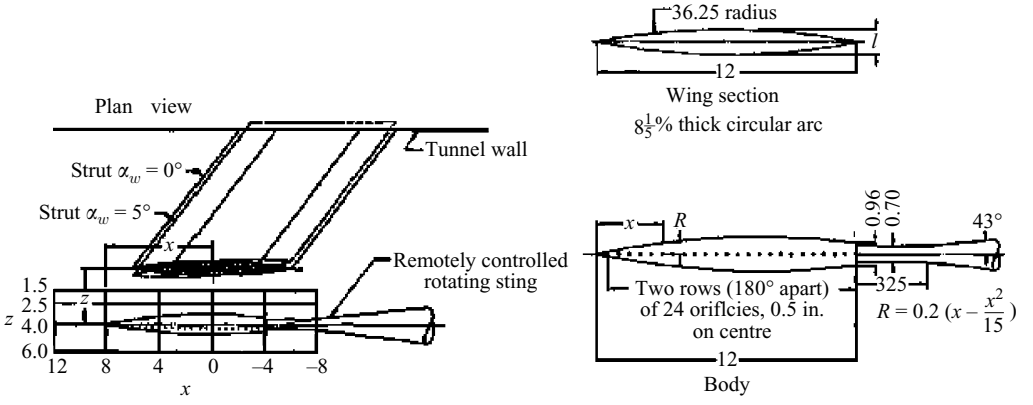

FIGURE 13. Schematic layout of test set-up and models (scanned from figure 1 of Gapcynski & Carlson 1957).

5% at $h/a = 3$ and quickly decreases as h/a increases. This behaviour is consistent with the theory indicating that the first scattering, which does not depend on h/a, produces the dominant effect.

5. Comparison with experiment

For further validation of the theoretical results we use the experimental data (Gapcynski & Carlson 1957) obtained in the Langley $4 \times 4\,\text{ft}^2$ supersonic wind tunnel. The aerodynamic characteristics of a body of revolution were measured in the two-dimensional flow field of a 25/3 % thick circular-arc wing of a rectangular plan form. Data were obtained at $M_\infty = 2.01$ and the free-stream unit Reynolds number $Re_{1\infty} = 3.6 \times 10^6\ \text{ft}^{-1}$. The test set-up is shown schematically in figure 13. The blunt-base parabolic body of revolution had the length $l^*_{PB} = 12$ in and the non-dimensional

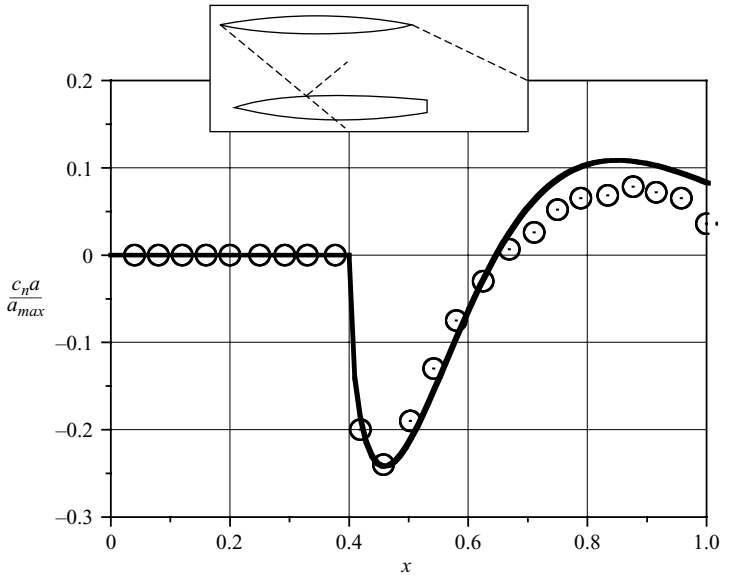

FIGURE 14. Comparison of theoretical (solid line) and experimental (symbols) distributions of the normal force induced by the wing shock impinging on the body at $x \approx 0.4$.

body radius $a(X) = 0.2(X - \frac{12}{15}X^2)$, $X = a^*/l^*_{PB}$. The wing has the chord length $l^*_w = l^*_{PB}$ and the arc radius $R^* = 36.25$ in. The wing arc is approximated well by a parabola $y(x) = \varepsilon(x - x^2)$ with $0 \leqslant x \leqslant 1$ and $\varepsilon = 1/6$.

The normal force distribution along the body axis is shown in figure 14 (symbols) for the case of the wing leading-edge shock impinging on the body at $x \approx 0.4$. In this plot

$$c_n \frac{a}{a_{max}} = \frac{1}{\rho^*_\infty U^{*2}_\infty a^*} \frac{\mathrm{d}L^*}{\mathrm{d}x^*} \frac{a}{a_{max}}, \tag{5.1}$$

where c_n is the cross-sectional normal force coefficient. Using the definition (3.1) we obtain

$$c_n \frac{a}{a_{max}} = \frac{\pi a}{2} c_L \frac{a}{a_{max}}. \tag{5.2}$$

In the case considered herein, there is only the first scattering and (3.23a, b) gives

$$c_L = \frac{8\varepsilon}{\pi(a\beta)^3} D^{(1)}(\bar{x}_1),\ D^{(1)}(\bar{x}_1) = L^{-1}_{\bar{p}} \left[\frac{\mathrm{i}\bar{F}(\bar{p}/\beta a)}{H^{(2)'}_1(-\mathrm{i}\bar{p})} \mathrm{e}^{-\bar{p}} \right], \tag{5.3}$$

where $\bar{F}$ is Laplace transform of $F(x) = x(1 - x)$, $0 \leqslant x \leqslant 1$,

$$\bar{F}(\bar{p}/\beta a) = \frac{\beta^2 a^2}{\bar{p}^2} \left[1 + \mathrm{e}^{-\bar{p}/\beta a} - 2\frac{\beta a}{\bar{p}} \left(1 - \mathrm{e}^{-\bar{p}/\beta a} \right) \right]. \tag{5.4}$$

Since βa is small, the exponential terms in (5.4) are omitted and the local lift coefficient is expressed as

$$c_L = \frac{8\varepsilon}{\pi a \beta} L^{-1}_{\bar{p}} \left[\frac{\mathrm{i}\mathrm{e}^{-\bar{p}} f(\bar{p}/\beta a)}{\bar{p}^2 H^{(2)'}_1(-\mathrm{i}\bar{p})} \right], \tag{5.5}$$

$$f(\bar{p}/\beta a) = 1 - 2\frac{\beta a}{\bar{p}}. \tag{5.6}$$

Substitution of (5.5) into (5.2) gives

$$c_n \frac{a}{a_{max}} = \frac{4\varepsilon}{\beta} \frac{a}{a_{max}} E(\bar{x}), \tag{5.7}$$

$$E(\bar{x}) = L_{\bar{p}}^{-1} \left[\frac{\mathrm{i} e^{-\bar{p}} f(\bar{p}/\beta a)}{\bar{p}^2 H_1^{(2)'}(-\mathrm{i}\bar{p})} \right], \qquad \bar{x} = (x - x_{sh})/\beta a. \tag{5.8}$$

Calculations were conducted using (5.6)–(5.8) with the parameters relevant to experimental conditions: $\varepsilon = 1/6$ and $\beta a \approx 0.0948$, where $a(x)$ is calculated at $x = x_{sh} = 0.4$.

As shown in figure 14, the theoretical distribution of the cross-sectional normal force coefficient (solid line) agrees well with the experimental data (symbols) in the region $0.4 \leqslant x \leqslant 0.65$. Further downstream, where the body radius varies significantly and the body surface is poorly approximated by a cylinder, the theoretical curve deviates from the experimental points. In general, the agreement is satisfactory, which demonstrates robustness of the analytical solution.

6. Concluding remarks

The lift force associated with multi-scattering of the wing-induced shock wave by a slender body of revolution was analysed using linearized supersonic theory, scattering theory and asymptotic methods. The local and integral lift coefficients were obtained in simple analytical forms convenient for quick calculations of aerodynamic loads. These solutions can be applied to the moderate supersonic (Mach numbers from 1.2 to 3) multi-body interaction problem for crosschecking with other computational or engineering methods.

The total lift coefficient, which is due to multiple scatterings of the wing leading-edge shock by a long cylinder, is concentrated near the station $x = \beta h$, where the shock crosses the body axis, and expressed in very simple form $C_L(\infty) = 4\varepsilon$. This force is predominantly generated by the first scattering. The second, third and higher scatterings do not contribute to the total lift in the leading-order approximation with respect to small parameter $\mu = a/2h$ characterizing the distance between the interacting bodies. On one hand, the analytical solution, which is inaccessible from purely numerical methods, shows the excellent complementarity of the numerics and the pen-and-paper methods. On the other, the numerics shows accessibility to nonlinear effects not modelled by the linear theory.

The analytical solution agrees satisfactory with the experimental data obtained for the blunt-base parabolic body of revolution in the flow field induced by a circular-arc wing in the Mach = 2 free stream, despite the facts that the body radius varies in the interaction region and the wing thickness is not very small ($\varepsilon = 1/6$). This adds more confidence to the practicability of the theoretical model.

The aforementioned conclusions are valid for bodies with slender sharp noses satisfying the constraint $\mu^{1/2}(a/l_N)^2 \ll \varepsilon$. Otherwise, the lift force due to scattering of the nose-induced disturbances should be taken into account. The solutions obtained can be treated as near-field solutions, describing scattering of the far-field disturbances in local regions of the order of body radius a. By matching the near-field and far-field solutions it is feasible to derive a composite asymptotic solution valid for a sufficiently broad class of configurations associated with the multi-body interaction problem. This is the subject of further analysis.

This work was supported by the Air Force of Scientific Research, Air Force Materials Command under Contracts F499620-99-0005, F499620-02-C-0024 and FA9550-05-C-0030. The US government is authorized to reproduce and distribute reprints for government purposes, notwithstanding any copyright notation thereon. The views and conclusions herein are those of the authors and should not be interpreted as necessarily representing the official policies or endorsements, either expressed, or implied of the Air Force Office of Scientific Research or the US government.

REFERENCES

Abramowitz, M. & Stegun, I. A. 1964 *Handbook of Mathematical Functions with Formulas, Graphs and Mathematical Tables*. National Bureau of Standards, Applied Mathematics Series 55.

Ashley, H. & Landahl, M. 1965 *Aerodynamics of Wings and Bodies*. Addison–Wesley.

Belk, D. M., Janus, J. M. & Whitfield, D. L. 1987 Three-dimensional unsteady Euler equations solution on dynamic grids. *AIAA J.* **25**, 1160–1161.

Bowman, J. J., Senior, T. B. A. & Uslenghi, P. L. E. 1969 *Electromagnetic and Acoustic Scattering by Simple Shapes*. North-Holland.

Chakravarthy, S. R. & Osher, S. 1985 A new class of high accuracy TVD schemes for hyperbolic conservation laws. *AIAA Paper* 85-0363.

Cole, J. D. & Cook, L. P. 1986 *Transonic Aerodynamics*. Elsevier, North-Holland.

Gapcynski, J. P. & Carlson, H. W. 1957 The aerodynamic characteristics of a body in the two-dimensional flow field of a circular-arc wing at a Mach number 2.01. *NACA Res. Mem.* L57E14.

Jordan, J. K. 1992 Computational investigation of predicted store loads in mutual interference flow fields. *AIAA Paper* 92-4570.

Landau, L. D. & Lifshitz, E. M. 1986 *Theoretical Physics*, vol. 6: *Hydrodynamics*. Nauka Moscow (in Russian).

Lependin, L. F. 1978 *Acoustics*. Vysshaya Shkola, Moscow (in Russian).

Loitsyansky, L. G. 1970 *Fluid and Gas Mechanics*. Nauka, Moscow (in Russian).

Malmuth, N. D. 2005 Theoretical aerodynamics in today's real world, opportunities and challenges. Julian D. Cole Lecture. *AIAA Paper* 2005-5059.

Morse, P. M. & Feshbach, H. 1953 *Methods of Theoretical Physics*, pp. 1376–1382, McGraw–Hill.

Prewitt, N. C., Belk, D. M. & Maple, R. C. 1999 Multiple-body trajectory calculations using the Beggar code. *J. Aircraft* **36**, 802–808.

Roe, P. L. 1986 Characteristic based schemes for the Euler equations. *Annu. Rev. Fluid Mech.* **18**, 337–365.

Shalaev, V. I., Fedorov, A. V. & Malmuth, N. D. 2004 Theoretical modeling of interaction of multiple slender bodies in supersonic flows. *AIAA Paper* 2004-1127.

Thoms, R. D. & Jordan, J. K. 1995 Investigation of multiple body trajectory prediction using time accurate computational fluid dynamics. *AIAA Paper* 95-870.

Van Dyke, M. 1964 *Perturbation Methods in Fluid Mechanics*. Academic.

Weiss, J. M., Maruszewski, J. P. & Smith, W. A. 1997 Implicit solution of the Navier–Stokes equations on unstructured meshes. *AIAA Paper* 97-2103.